PRELIMINARY STUDY OF CEDBT AND CESM PERFORMANCES USING SIMULATED ANALYTICAL CONTRAST UPTAKES

R. Sánchez de la Rosa[*†], *A.-K. Carton*[*], *P. Milioni de Carvalho*[*], *Z. Li*[*], *S. Muller*[*], *I. Bloch*[†]

[*]GE Healthcare, Buc, France
[†]LTCI, Télécom ParisTech, Université Paris-Saclay, Paris, France

ABSTRACT

Contrast Enhanced Spectral Mammography (CESM) delivers in one single exam both morphological information and contrast uptakes of hyper-vascularized tissues in breasts, providing better diagnosis performance for breast cancer than diagnostic mammography. Contrast-Enhanced Digital Breast Tomosynthesis (CEDBT), with the association of Digital Breast Tomosynthesis (DBT), providing volumetric description of the anatomy, and CESM, providing contrast uptake information, is expected to increase localization and characterization of contrast uptakes. In this study, we introduce a new simulation method to generate mass-like enhancements from analytically defined structures. A preliminary human observer evaluation, comparing performances of CESM versus central CEDBT slices, was conducted, focusing on detectability and characterization of mass-like contrast enhancements combining different ACR BIRADS descriptors. Central CEDBT slices improve characterization of shape and margin, while CESM shows better performance in defining contrast enhancement distribution inside mass-like uptakes. Further studies are necessary to refine the benefits of CEDBT using entire sets of slices.

Index Terms— Lesion simulation, Contrast Enhanced Spectral Mammography, Contrast Enhanced Digital Breast Tomosynthesis, detection and characterization evaluation.

1. INTRODUCTION

Breast tumor growth and metastasis are concomitant with the development of new blood vessels presenting an abnormal increased permeability [1]. As a result, the contrast agent intravenously injected to the patient is often leaking in the interstitial tissue of malignant breast lesions fed by these poor-quality vessels. Using gadolinium chelates as a vascular contrast agent, 3D contrast-enhanced magnetic resonance imaging (CE-MRI) is the current standard providing functional breast images, and thus allows for detection of abnormal vascular development and lesion contrast uptake. Using an iodinated contrast-agent injection, contrast-enhanced spectral mammography (CESM) is a recently introduced dual-energy X-ray imaging application providing similar functional lesion information but at lower cost [2]. CESM is however a projection technique providing 2D images of the breast. It is expected that a three-dimensional contrast-enhanced X-ray imaging technique could provide improved lesion localization and contrast-agent uptake characterization, resulting in a potentially improved specificity [3]. We believe that

contrast-enhanced digital breast tomosynthesis (CEDBT), a multi-energy X-ray technique whereby 3D tomographic sections of the breast, both morphological and functional, are reconstructed from a set of projection images acquired from different X-ray tube viewpoints, is a good candidate to achieve this goal [4]. However, its incremented clinical value, compared to the current CESM exam, is still not well understood [5].

The BIRADS lexicon, previously introduced for 3D CE-MRI [6], allows for a clear description of contrast enhancements, including lesion shape, margin and enhancement pattern. Similarly, a BIRADS lexicon for CESM is underway [7]. Due to the lack of a complete database of characterized lesions for both methodologies and to better understand the potential value of CEDBT versus CESM, we propose to compare lesion description performance in CESM and CEDBT images using a simulation platform. In this work, we introduce a method to model iodine-enhancing breast lesions with various morphological characteristics encountered in clinical practice. These lesions were then embedded in a previously developed breast texture model [8] and imaged with a previously introduced breast X-ray imaging platform [9]. Finally, we present a preliminary human observer experiment whereby the lesion detection and characterization performances of simulated CESM and CEDBT images were compared using BIRADS criteria.

Mass		Non Mass	
Shape	Round	Pattern	Focal
	Oval		Linear
	Irregular		Segmental
Margin	Sharp		Regional
	Indistinct		Multiple Regions
	Spiculated		
Enhancement	Homogeneus	Enhancement	Diffuse
	Heterogeneus		Homogeneous
	Rim Enhancement		Heterogeneous
			Clumped
	Dark Internal Septa		Clustered ring

Table 1. Descriptors used for characterizing lesions in CESM and CE-MRI images.

2. CONTRAST-ENHANCED LESION SIMULATION

A software platform was created to generate mass-like lesions exhibiting typical characteristics encountered in clinical CE-MRI and CESM imaging (Table 1). Lesions are defined analytically by multiple geometric primitives. Each geometric primitive is assigned a (different) material composition. To compute images of the simulated lesions, an analytical ray-tracing projector is used [10]. Each geometric primitive constitutive of the lesion is read according to an ordered set, whereby the material attenuation coefficients of previously read primitives are overwritten by those of subsequent primitives. More precisely, the lesion generation occurs in three steps.

Step 1 – Lesion shape: Round, oval and irregular lesions are defined by a central sphere or ellipsoid. For irregular lesions, their surface is further deformed as follows. A configurable number of seed points is positioned on the sphere or ellipsoid surface according to an uniform distribution. Each seed point is the center of a new sphere or ellipsoid. The number of seed points is typically set to 30. The orientation and size of the peripheral primitives are uniformly distributed. Their size is similar to the dimensions of central lesion.

Step 2 – Lesion margin: Margin of lesions with sharp margins are not modified. To design indistinct margins, we considered that iodine concentration decreases from the lesion core towards the lesion surface, while preserving the original lesion envelope generated in step one. A series of smaller concentric geometric primitives with linearly increasing iodine concentration towards the lesion center is then generated within the lesion envelope. The number of added primitives is proportional to the lesion size and iodine concentration. To define spiculated margins, a number of seed points is uniformly distributed on the lesion envelope. Then, a right circular cone is placed tangentially to the surface on each seed point, the base of each cone being included inside the lesion envelope to preserve continuity. The cone height and base diameter are set to 2.4 cm and 0.05 cm, respectively, and the number of spicules is typically set to 40. These numbers were defined as baseline limitation to detect spicules.

Step 3 – Iodine enhancement: For homogeneous lesions, all the elements constituting the lesion share the same iodine concentration. Indistinct lesions are not further modified, since they were considered in Step 2 to be characterized by a heterogeneous enhancement pattern. To model heterogeneous iodine enhancement, spheres are positioned along several axes extending from the lesion center towards the lesion surface. Sphere diameters increase from the lesion center towards the lesion surface. To model gradually changing iodine enhancement, iodine concentrations assigned to each spherical primitive are computed using an inverse distance weighting approach with respect to a set of reference positions with pre-defined iodine concentrations [11]. As an example, to model an 8-mm diameter heterogeneously enhancing spherical lesion, 113 000 additional spheres are created to build a discrete enhancing distribution with a step smaller than the pixel size in the detector. Rim enhancements and dark internal septa are created by inserting a concentric core of non-iodine enhancing breast tissue inside the original structure envelope (i.e. percentage of adipose plus glandular tissue).

Each lesion is described in FORBILD text file syntax (Institute of Medical Physics, Erlangen, Germany)[1]. The framework to gener-

---

[1] http://www.imp.uni-erlangen.de/forbild/

Shape	Margin	Enhancement	Size [cm]: 0.8	Volumetric concentration [mg /cm³]	# texture backgrounds
Round	Sharp	Homogeneous		0.3 & 0,5	5
				1	1
		Heterogeneous		0.3 & 0,5	5
				1	1
		Rim	Thickness rim: 0.143	0,6 & 1 (*)	5
				2	1
		Internal Septa		0.3 & 0.5	5
				1	1
	Spiculated	Homogeneous	Spicules: Length = 2.4 Width = 0.05 # = 40	0.3 & 0.5	5
				1	1
	Indistinct	Heterogeneous		0.3 & 0.5	5
				1	1
Oval	Sharp	Homogeneous	Min axis: 0.8 Max axis: 1.2 (randomize rotation axis)	0.3 & 0.5	5
				1	1
Irregular	Sharp	Homogeneous		0.3 & 0.5	5
				1	1

Table 2. Lesion characteristics used in this study. (*) Contrast concentration of rim enhancement lesions was increased to preserve a similar surface concentration in CESM projections.

ate the lesions was implemented in Matlab and the computation time depends on the descriptors required to simulate a particular lesion. For the structures generated in this study about 1 minute per lesion was required (using Intel® Xeon® CPU ES-2630 v2 @ 2.60GHz).

3. HUMAN OBSERVER EXPERIMENT

Image data set: To assess detection and characterization of iodine-enhancing mass lesions, 88 CESM and 88 CEDBT images with mass lesions were generated. The morphological features, dimensions, iodine concentrations and number of the studied lesion types are summarized in Table 2. Three different iodine concentrations, aiming to provide easy, moderate and difficult detection levels, were considered. Additionally, 30 CESM and 30 CEDBT images without lesions were included in the evaluation. The masses were embedded in the center of 5-cm thick voxelized simulated textured breast phantoms (voxel size: $0.1 \times 0.1 \times 0.1$ mm), generated according to a previously published method [8]. The textured breast phantoms had a 27% average glandular density. To simulate Breast Parenchymal Enhancement (BPE) seen in clinical CESM images, a homogeneous mixture of fibroglandular tissue and a $0.1 mg/cm^3$ iodine concentration was assigned to the fibroglandular voxels.

Image simulation: Image acquisitions were simulated using a previously described breast X-ray imaging simulation platform [9, 10]. CESM and CEDBT images were simulated according to the nominal topologies of respectively commercial CESM and DBT imaging systems (SenoBright HD and Senographe Pristina, GE Healthcare, Chalfont St Giles, UK). Mono-energetic primary X-rays were considered (22 keV for the low-energy (LE), and 34 keV for the high-energy (HE) images). Quantum noise and detector modulation transfer function were modeled. The total LE and HE quantum flux used for the CEDBT projections was the same as for the LE and HE CESM projections. The flux was tuned to match the signal-to-noise ratio (SNR) in real CESM images of a 5cm thick uni-
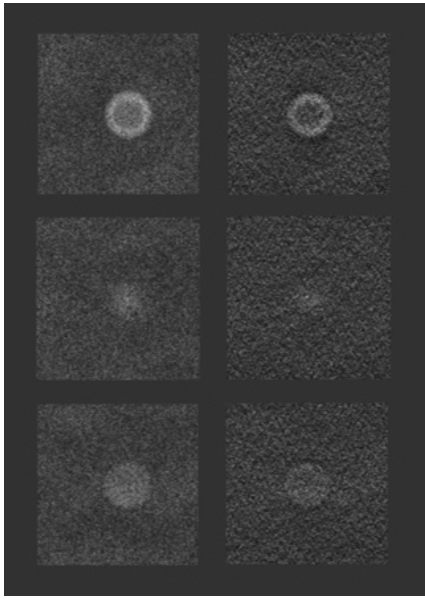
Fig. 1. Left: CESM projections. Right: CEDBT central slices. From top to bottom rows: rim, indistinct and heterogeneous enhancements, with the highest iodine concentrations used in this study.

form breast-equivalent section acquired with the automatic exposure mode. Other physical processes that are part of image formation in real x-ray imaging systems, such as lag, scatter and electronic noise, were not included in this study.

Iodine-enhancement images were then produced by recombining the LE and HE images [12]. An adaptive statistical iterative reconstruction (ASIR) method developed by GE Healthcare was used to compute the CE-DBT slices from the set of recombined projections. In this study, a preliminary 2D to 2D performance evaluation is based on the central slice of each CEDBT volume, where the diameter of the mass lesion is maximum, was shown to the readers.

Image review: Three GE Healthcare engineers, experts in mammography imaging but unrelated to the lesion simulation platform development, participated in the observer experiment. Reading sessions were conducted in a darkened room on a 5-Megapixel monitor. For each trial, a CESM or CEDBT image was randomly selected (examples in Figure 1). Images were presented at 100% resolution. Contrast, brightness and zoom levels were fixed. Between two consecutive trials, a uniform gray level image was displayed to minimize the visual influence of the previous image on scoring.

For each trial, five questions were asked to assess lesion detection and characterization performance:

Q1: Is there a lesion? (Yes / No)
Q2: What is the shape of the mass? (Round / Oval / Irregular)
Q3: How can you describe its margins? (Circumscribed / Indistinct / Spiculated)
Q4: How can you describe the distribution of its contrast enhancement? (Homogeneous / Heterogeneous / Rim)
Q5: What is the size of the longest diameter of the mass? (in mm)

A 4-level confidence rating scale was used for questions 1 to 4: Not confident at all (1), Not very confident (2), Confident (3), and

		Sensitivity			Specificity
		Global	Easy	Moderate	Difficult	
CESM	R1	0.78	1	1	0.53	0.97
	R2	0.85	1	0.98	0.7	0.93
	R3	0.8	1	0.98	0.6	1
CEDBT	R1	0.69	0.87	0.65	0.25	1
	R2	0.82	1	0.85	0.5	1
	R3	0.74	1	0.73	0.3	1

Table 3. Detectability task results for readers R1, R2 and R3.

Very confident (4). No time limitation was imposed on the observer to make a decision. A short training session preceded the actual trials; the questionnaire was explained and image projections of lesion primitives only were reviewed.

Data analysis: The detection performance was evaluated using the sensitivity and specificity ratios for all three readers. Also, sensitivity values for the three different contrast uptakes present in this study were studied separately.

For the characterization task, we calculated the rate between the number of correctly associated descriptors for a given image and the total number of times that the descriptor was present in the detected masses, in order to keep characterization separated from detectability. Confidence level for each descriptor was also considered.

4. RESULTS

This preliminary study showed a higher sensitivity for CESM and better specificity in CEDBT (Table 3). In CESM, the global value of sensitivity was impacted by the decrease of detectability seen for the smallest concentrations of contrast uptakes ($0.3mg/cm^3$). On the other hand, CEDBT showed a decreasing trend from the moderate iodine concentration ($0.5mg/cm^3$) with a larger drop for the smallest concentrations.

We observe in Table 4 that CEDBT yielded a higher correct characterization of shape descriptors, with an increased performance to describe round and irregular masses, and a similar ratio for oval contrast uptakes. Furthermore, circumscribed and spiculated masses were also better characterized using CEDBT, however, for indistinct contrast uptakes, there was no consensus between the three readers. Contrast enhancement distribution was generally better characterized in CESM, with a higher performance for heterogeneous and septa lesions, and a similar ratio for rim contrast uptakes. Homogeneous lesions were better characterized by CEDBT.

Confidence levels in characterization were poor due to small sensitivity in detection of low simulated iodine concentrations for both techniques (i.e. mean confidence value for all type of mass-like enhancement and readers equal to 2.6 and 2.4 for CESM and CEDBT respectively). This was translated into an important decrease in characterization values when only 3 and 4 confidence levels are considered.

5. DISCUSSION AND CONCLUSION

In this work, we proposed a new simulation environment to generate mass-like contrast uptakes using analytically defined objects, embedded in an anthropomorphic phantom, and simulate Low- and

		Shape			Margin			Enhancement			
		Round	Oval	Irregular	Circumscribed	Indistinct	Spiculated	Homogeneous	Heterogeneous	Rim	Septa
CESM	R1	55% (29/53)	60% (6/10)	50% (3/6)	83% (44/53)	33% (3/9)	0% (0/7)	70% (23/33)	24% (3/17)	73% (8/11)	25% (2/8)
	R2	64% (37/55)	70% (7/10)	0% (0/7)	63% (35/56)	60% (6/10)	11% (1/9)	61% (22/36)	37% (7/19)	64% (7/11)	22% (2/9)
	R3	56% (30/54)	100% (11/11)	33% (2/6)	34% (18/53)	89% (8/9)	11% (1/9)	54% (19/35)	76% (17/13)	91% (10/11)	50% (4/8)
CE-DBT	R1	77% (27/35)	57% (4/7)	100% (1/1)	94% (30/32)	60% (6/10)	33% (2/6)	89% (17/19)	57% (4/7)	91% (10/11)	0% (0/6)
	R2	82% (37/45)	56% (5/9)	50% (2/4)	60% (27/45)	33% (2/6)	29% (2/7)	81% (21/26)	18% (2/11)	64% (7/11)	0% (0/10)
	R3	86% (33/38)	100% (6/6)	60% (3/5)	50% (19/38)	100% (4/4)	29% (2/7)	77% (17/22)	25% (3/8)	91% (10/11)	0% (0/8)

Table 4. Percentages of lesions correctly characterized. The numbers between brackets are the ratios between the detected lesions characterized with the right descriptor and the total number of lesions of that type that are detected.

High-energy projections to generate CESM and CEDBT images. We also presented a preliminary human observer experiment to assess detection and characterization performance for both methodologies.

From the results we obtained, CESM seems to offer a better sensitivity for all three iodine contrast levels. However, when lesions are detected, CEDBT shows a superior characterization of the shape and margins of masses, with a higher performance to describe homogeneous contrasts uptakes. The results for the characterization of heterogeneous distributions and septations inside the lesions in CEDBT central slices could be negatively impacted by the absence of the complete stack of reconstructed slices that would be available to the radiologist in a clinical environment. Indeed, mass-like enhancements are present in multiple planes, providing more information than the single central slice used in our human observer experiment. Analyzing the complete set of CEDBT slices will be the aim of future studies.

The three contrast levels used in this study are below the iodine concentrations typically encountered in clinical CESM images, and they were deliberately chosen to achieve the limitations of both techniques. Consequently, sensitivity results could be impacted by this choice. A higher variability of iodine concentrations must be considered for future work. Also, the decision of GE engineers as human observers was motivated by the simplicity of the visual task, where the location of the possible lesions was always known. But a bias to real clinical performance needs to be considered.

Prior to this study, the physical processes contribution to image formation of the X-ray image simulation platform were adapted. In particular, the real imaging system signal response as a function of spatial frequency and the SNR properties were modeled to produce images with the same frequency and noise content. However, for this study, other processes such as lag, scatter, and electronic noise formation were not taken into account. The implementation of these additional elements could introduce new differences between both modalities, and will be the aim of our future work.

6. REFERENCES

[1] N Weidner, J P Semple, W R Welch, and J Folkman, "Tumor angiogenesis and metastasiscorrelation in invasive breast carcinoma," *New England Journal of Medicine*, vol. 324, no. 1, pp. 1–8, 1991.

[2] M Skarpathiotakis, M J Yaffe, A K Bloomquist, D Rico, S Muller, A Rick, and F Jeunehomme, "Development of contrast digital mammography," *Medical Physics*, vol. 29, no. 10, pp. 2419–2426, 2002.

[3] C Dromain, C Balleyguier, S Muller, M-C Mathieu, F Rochard, P Opolon, and R Sigal, "Evaluation of tumor angiogenesis of breast carcinoma using contrast-enhanced digital mammography," *American Journal of Roentgenology*, vol. 187, no. 5, pp. W528–W537, 2006.

[4] A-K Carton, SC Gavenonis, JA Currivan, EF Conant, MD Schnall, and ADA Maidment, "Dual-energy contrast-enhanced digital breast tomosynthesis – a feasibility study," *The British Journal of Radiology*, vol. 83, no. 988, pp. 344–350, 2010.

[5] C-P Chou, J M Lewin, C-L Chiang, B-H Hung, T-L Yang, J-S Huang, J-B Liao, and H-B Pan, "Clinical evaluation of contrast-enhanced digital mammography and contrast enhanced tomosynthesis – comparison to contrast-enhanced breast mri," *European Journal of Radiology*, vol. 84, no. 12, pp. 2501–2508, 2015.

[6] C J D'Orsi, *ACR BI-RADS Atlas: Breast Imaging Reporting and Data System*, American College of Radiology, 2013.

[7] R M Kamal, M H Helal, S M Mansour, M A Haggag, O M Nada, I G Farahat, and N H Alieldin, "Can we apply the mri bi-rads lexicon morphology descriptors on contrast-enhanced spectral mammography?," *The British Journal of Radiology*, vol. 89, no. 1064, pp. 20160157, 2016.

[8] Z Li, *Task-based optimization of 3D breast X-ray imaging using mathematical observers*, Ph.D. thesis, Université Paris-Saclay, 2017.

[9] P Milioni de Carvalho, *Low-dose 3D quantitative vascular X-ray imaging of the breast*, Ph.D. thesis, Paris 11, 2014.

[10] B De Man, S Basu, N Chandra, B Dunham, P Edic, M Iatrou, S McOlash, P Sainath, C Shaughnessy, B Tower, et al., "CatSim: a new computer assisted tomography simulation environment," in *Proc. SPIE*, 2007, vol. 6510, p. 65102G.

[11] D Shepard, "A two-dimensional interpolation function for irregularly-spaced data," in *Proceedings of the 1968 23rd ACM national conference*. ACM, 1968, pp. 517–524.

[12] S Puong, X Bouchevreau, F Patoureaux, R Iordache, and S Muller, "Dual-energy contrast enhanced digital mammography using a new approach for breast tissue canceling," in *Medical Imaging*. International Society for Optics and Photonics, 2007, pp. 65102H–65102H.